ARTICLE

Efficient upgrading of CO to C_3 fuel using asymmetric C-C coupling active sites

Xue Wang [1,8], Ziyun Wang [1,8], Tao-Tao Zhuang[1], Cao-Thang Dinh [1], Jun Li [1,2], Dae-Hyun Nam [1], Fengwang Li [1], Chun-Wei Huang[3], Chih-Shan Tan[1], Zitao Chen [4], Miaofang Chi [4], Christine M. Gabardo [2], Ali Seifitokaldani [1], Petar Todorović[1], Andrew Proppe [1,5], Yuanjie Pang[1,2], Ahmad R. Kirmani[6,9], Yuhang Wang [1], Alexander H. Ip[1], Lee J. Richter[6], Benjamin Scheffel[1], Aoni Xu[1], Shen-Chuan Lo[3], Shana O. Kelley [5,7], David Sinton [2] & Edward H. Sargent [1]*

The electroreduction of C_1 feedgas to high-energy-density fuels provides an attractive avenue to the storage of renewable electricity. Much progress has been made to improve selectivity to C_1 and C_2 products, however, the selectivity to desirable high-energy-density C_3 products remains relatively low. We reason that C_3 electrosynthesis relies on a higher-order reaction pathway that requires the formation of multiple carbon-carbon (C-C) bonds, and thus pursue a strategy explicitly designed to couple C_2 with C_1 intermediates. We develop an approach wherein neighboring copper atoms having distinct electronic structures interact with two adsorbates to catalyze an asymmetric reaction. We achieve a record n-propanol Faradaic efficiency (FE) of $(33 \pm 1)\%$ with a conversion rate of $(4.5 \pm 0.1)\,\mathrm{mA\,cm^{-2}}$, and a record n-propanol cathodic energy conversion efficiency ($EE_{\mathrm{cathodic\ half\text{-}cell}}$) of 21%. The FE and $EE_{\mathrm{cathodic\ half\text{-}cell}}$ represent a 1.3× improvement relative to previously-published CO-to-n-propanol electroreduction reports.

[1] Department of Electrical and Computer Engineering, University of Toronto, 35 St George Street, Toronto, ON M5S 1A4, Canada. [2] Department of Mechanical and Industrial Engineering, University of Toronto, 5 King's College Road, Toronto, ON M5S 3G8, Canada. [3] Material and Chemical Research Laboratories, Industrial Technology Research Institute, Hsinchu 31040, Taiwan. [4] Center for Nanophase Materials Sciences, Oak Ridge National Laboratory, 1 Bethel Valley Road, Oak Ridge, TN 37830, USA. [5] Department of Chemistry, University of Toronto, 80 St George Street, Toronto, ON M5S 3H6, Canada. [6] Materials Science and Engineering Division, National Institute of Standards and Technology (NIST), 100 Bureau Dr, Gaithersburg, MD 20899, USA. [7] Department of Pharmaceutical Sciences, Leslie Dan Faculty of Pharmacy, University of Toronto, 144 College Street, Toronto, ON M5S 3M2, Canada. [8] These authors contributed equally: Xue Wang, Ziyun Wang. [9] Guest researcher *email: ted.sargent@utoronto.ca

The CO_2 electroreduction reaction (CO_2RR) to high-energy-density liquid products is an attractive avenue to achieving the storage of renewable energy. In recent years, much progress has been made in CO_2RR, but the main products reported have been C_1 (CO, CH_4, methanol, and formate) and C_2 (ethylene, acetate, and ethanol) products[1–13]. n-propanol, a high-value and high-energy-density C_3 product that can be generated via either CO_2 or CO electroreduction[14,15], has been produced with low-to-moderate Faradaic efficiencies (FEs) in prior reports[10,12,16–26].

In CO_2RR, the formation of multi-carbon products starts with the formation of the CO intermediate, followed by the CO electroreduction process[27–29]. Recently, significant progress has been made in CO_2RR to CO with a FE nearly 100%[30–32]. To achieve the ultimate goal of high selectivity to high-value-added C_3 products from CO_2RR, it is of interest to improve significantly the FE for CO electroreduction (CORR) to C_3 products.

The formation of C_3 products from CORR relies on the sequential formation of two carbon–carbon (C–C) bonds, the main reaction mechanism for C_3 formation reported previously[25,33,34]. Cu provides excellent C–C coupling and produces multi-carbon chemicals in the electroreduction of CO; however, the selectivity towards C_3 products on Cu has remained low[35,36]. The generation of C_3 products from CO requires multiple product/intermediate formation steps, and it is prone to the competing production of a wide variety of chemical products[33,34,37,38].

Increasing selectivity in the electroreduction of CO to C_3 products is thus an important challenge to address in the field of electrocatalysis. Until now, catalysts for CORR have focused on Cu and oxide-derived Cu catalysts, and a number of factors have been found to increase performance: these include engineering the oxidation state of the atoms making up the metal catalyst, as well as grain-boundary effects and the selective formation of desired facets[16,21–26,39]. However, the main products of these Cu and oxide-derived Cu catalysts have been C_2 chemicals (ethanol, acetate, and ethylene), and the selectivity to C_3 products has saturated in recent manuscripts based on Cu catalysts.

Here we explore instead a doping strategy involving different metal-doped Cu (M-doped Cu) catalysts in an attempt to increase C_3 production in CORR. The low C_3 selectivity on Cu catalysts is associated with the low rate of C–C bond formation, including C_1–C_1 and C_1–C_2 coupling. Mechanisms underpinning C_1–C_1 coupling to C_2 products have been explored extensively in prior studies[29,33,38,40–42]; while C_1–C_2 coupling to C_3 products is less

explored. Here we screen the propensity to catalyze C_1–C_1 and C_1–C_2 coupling using density functional theory (DFT) based on M-doped Cu catalysts. We find that, among different M-doped Cu candidates explored, Ag-doped Cu is expected to offer the highest activity for both C_1–C_1 and C_1–C_2 coupling, and we pinpoint a role for the asymmetric C–C coupling active site in this high activity. Specifically, this active site consists of two neighboring Cu atoms that exhibit different electronic structures: this asymmetry among the neighbors' energetics is determined by the combination of strain and ligand effects arising upon Ag doping. We then fabricate Ag-doped Cu nanocatalysts via a galvanic replacement approach. We demonstrate that the synthesized Ag-doped Cu catalyst exhibits higher FEs for n-propanol compared to all previous CORR reports[10,12,16–26]. This leads to superior energy conversion efficiency in the cathodic half-cell ($EE_{cathodic\ half-cell}$) for n-propanol.

Results

Computational modeling and catalyst design principles. Catalysts that convert CO into C_3 chemicals require high activity for both C_1–C_1 and C_1–C_2 coupling. With the goal of designing better catalysts for C_3 production, we investigated the energetics of C_1–C_1 and C_1–C_2 coupling reactions to illustrate the C_2 and C_3 formation rates with the aid of DFT (more details of DFT methods and choice of sequential mechanism can be found in Supplementary Information). Several M-doped Cu systems (M = Ag, Au, Ru, Rh, and Pd) were considered because bimetallic catalysts have been shown to tune catalyst performance in other catalytic reactions[43,44]. CO dimerization is one reaction pathway for C_1–C_1 coupling[29,40], so we used the barrier of CO dimerization to describe the readiness of C_1–C_1 coupling. Due to the abundance of CO species in CORR, we used the barrier of OCCO and CO coupling as the indicator for the C_1–C_2 coupling (Supplementary Figs. 1–14 and Supplementary Tables 1–3). As shown in Fig. 1a, among the M-doped Cu systems studied, calculation results show that Ag-doped Cu possesses the lowest activation energies for both C_1–C_1 and C_1–C_2 coupling, suggesting that Ag-doped Cu is a promising catalyst for the formation of C_3 products from CO.

We carried out further theoretical investigations to uncover the physical origins of enhancement in C_1–C_1 and C_1–C_2 coupling on Ag-doped Cu. We used a model with one Ag atom doped in a Cu (111) slab with a 3×3 unit cell, which corresponds to about 3% doping concentration for four layers of Cu atoms. By a margin of 0.63 eV, Ag at the surface of Cu(111) is more favorable than in
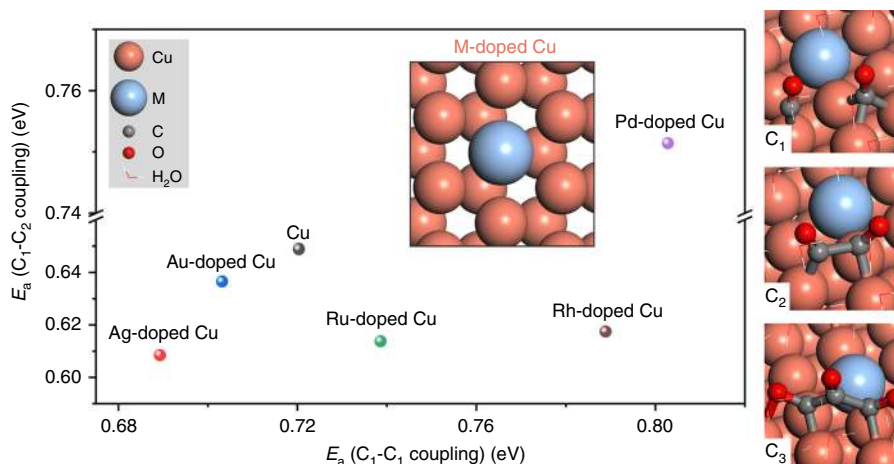
Fig. 1 DFT calculations on C_1–C_1 and C_1–C_2 coupling. DFT calculated reaction barriers (E_a) for C_1–C_1 and C_1–C_2 coupling on screened M-doped Cu systems (M = Ag, Au, Ru, Rh, and Pd). The geometries of M-doped Cu surface, C_1, C_2, and C_3 on M-doped Cu are shown with the corresponding labels, respectively. Cu, M, C, and O are illustrated as orange, light blue, gray, and red balls, respectively, while water molecules are shown as lines

subsurface of Cu(111), inducing us to focus on surface-localized Ag in our ensuing studies.

As the radius of the Ag atom is larger than that of Cu atom, Ag doping produces surface strain. The bond length of Cu–Cu changed from 2.57 Å on the Cu(111) surface to 2.55 and 2.48 Å on the Ag-doped Cu surface, resulting in asymmetric compressive strain (Supplementary Fig. 15). The ligand effect[45] caused by Ag doping in Cu also has the potential to affect C_1–C_1 and C_1–C_2 coupling. To evaluate the effect of the strain and ligand, we built a model with the same strain of Ag-doped Cu but without Ag substitution by fixing the bond length of Cu surface (denoted *Cu with strain*). We calculated the activation energies for C_1–C_1 and C_1–C_2 coupling steps on Cu, Cu with strain, and Ag-doped Cu models (Supplementary Table 4). Calculation results show that both compressive strain and ligand effects contribute to enhanced activity for C_1–C_1 and C_1–C_2 coupling (Supplementary Fig. 16a).

Ag doping in Cu leads to two classes of neighboring Cu atoms (denoted Cu-a and Cu-b atoms, Supplementary Fig. 16b). The two classes exhibit distinct electronic structures, as a result of strain and ligand effects. As to the strain effect, the bond length between Cu-a and Cu-b atoms is 2.55 Å, while the bond length between two Cu-b atoms is 2.48 Å (Supplementary Fig. 15), suggesting that Cu-a is more isolated than Cu-b. As to ligand effects, Cu-a coordinates with nine Cu atoms, while Cu-b coordinates with eight Cu atoms and one Ag atom (Supplementary Fig. 16). We term a pair of adjacent Cu atoms with different electronic structures an *asymmetric C–C coupling active site*. In this reaction, the asymmetric site interacts with two CO to yield asymmetric reactants—two adsorbed CO on Cu-a and Cu-b atoms with different electronic structures—enhancing C_1–C_1 coupling. In light of the similarity with C–C coupling, the same site can further promote C_1–C_2 coupling between asymmetric C_1 and C_2 intermediates (Supplementary Fig. 17). These findings are in ways analogous to the enhanced coupling effect of Cu^0 and Cu^+ proposed by Goddard and co-workers[41]. Taken together, these DFT calculation results suggest that Ag-doped Cu with asymmetric C–C coupling active sites is a good candidate for C_3 production in CORR which appear to support both C_1–C_1 dimerization and C_1–C_2 coupling. It is worth mentioning that there exist other C_1–C_2 coupling possibilities: we also examined another C_1–C_2 coupling mechanism, OC-OCCOH (refs. [33,39]), and found that Ag-doped Cu had a barrier of 0.76 eV, lower than 0.88 eV on Cu (Supplementary Figs. 18, 19, and Supplementary Table 5).

Preparation and characterization of nanocatalysts. We sought to prepare experimentally Ag-doped Cu catalysts. We employed a galvanic replacement reaction driven by the difference in the reduction potential of Ag vs. Cu (ref. [46]). Firstly, we deposited a thin layer of commercial Cu nanoparticles with average size of 100 nm on a carbon-based gas diffusion layer (GDL) via spray-coating (Supplementary Fig. 20a). The Cu gas diffusion electrode (GDE) was then immersed in N_2-saturated 5 µmol L^{-1} $AgNO_3$ aqueous solution at 65 °C for 1 h to obtain the Ag-doped Cu GDE. The Ag-doped Cu catalyst retains the particle size and the morphology of the pristine Cu nanoparticles (Fig. 2a, b, and Supplementary Figs. 20 and 21). Electron energy loss spectroscopy (EELS) elemental mapping showed that Ag and Cu elements were uniformly distributed in the particle (Fig. 2c and Supplementary Fig. 22). In transmission wide angle X-ray scattering (WAXS) data and powder X-ray diffraction (XRD) patterns, we observed peaks for Cu_2O in both Cu and Ag-doped Cu GDE (Fig. 2d, e, and Supplementary Fig. 23), which were attributed to oxidation of Cu in air during the preparation of GDE. Due to the low concentration of Ag (4.0% atomic fraction

determined by XPS), a peak shift relative to Cu is not observed in WAXS data of the Ag-doped Cu GDE (Fig. 2e and Supplementary Table 6). X-ray photoelectron spectroscopy (XPS) of the Ag-doped Cu GDE also showed the existence of CuO on the surface and confirmed the presence of Ag^0 (Fig. 2f, g).

CORR performance and Operando X-ray absorption spectroscopy. We then investigated the performance of the Ag-doped Cu GDE in CORR flow cell reactors (Supplementary Fig. 24). Flow cells overcome the mass transfer limitation of CO and produce a triple-phase interface that allows the gas reactant to contact the catalyst-electrolyte interface during the reaction. Figure 3a shows FEs for C_{2+} products in the applied potential range of −0.36 to −0.56 V with reference to the reversible hydrogen electrode (RHE) in 1 M KOH electrolyte. The liquid products (*n*-propanol, ethanol, and acetate) and gas products (ethylene and H_2) were quantified using nuclear magnetic resonance (NMR) and gas chromatography, respectively (Supplementary Fig. 25 and Supplementary Table 7). In the applied potential range of −0.36 to −0.56 V_{RHE}, the total C_{2+} FEs on Ag-doped Cu GDE are higher than that on Cu GDE: indeed the total FE of C_{2+} products on Ag-doped Cu GDE reaches about 80% at -0.56 V_{RHE}. In particular, at a low potential of −0.46 V_{RHE}, the Ag-doped Cu GDE records a high *n*-propanol FE of $(33 \pm 1)\%$ with the partial *n*-propanol current density of (4.5 ± 0.1) mA cm^{-2}, whereas *n*-propanol FE on pristine Cu is $(22 \pm 1)\%$ (Fig. 3b). This impressive *n*-propanol FE represents the highest value reported for *n*-propanol production via CO_2RR and CORR (Supplementary Table 8). The higher FE for C_{2+} and C_3 products on Ag-doped Cu relative to Cu is consistent with predictions from DFT. The intrinsic activities for *n*-propanol production on Ag-doped Cu and Cu are reported via the partial current density for *n*-propanol production normalized to the electrochemical surface area (ECSA) (Supplementary Figs. 26, 27, and Supplementary Table 9). The ECSA-normalized partial *n*-propanol current density on Ag-doped Cu is 0.124 mA cm^{-2}, which is 3 times that on Cu. The *n*-propanol $EE_{cathodic\ half-cell}$ reaches 20% at a low potential of −0.46 V_{RHE} when the overpotential of oxygen evolution in anode side is assumed to be 0. After correcting for ohmic loss (Supplementary Table 10), the *n*-propanol $EE_{cathodic\ half-cell}$ reaches 21% under a low overpotential of 0.616 V. This $EE_{cathodic\ half-cell}$ is higher than the best prior reports by a margin of 1.3× (Supplementary Sections 3, 4, and Supplementary Table 8).

It should be noted that the highest *n*-propanol FE on both Ag-doped Cu and Cu GDEs were achieved at relatively low potential (-0.46 V_{RHE}), and *n*-propanol FE decreased when further increasing the potential to −0.56 V_{RHE} (Fig. 3a and Supplementary Table 7). The total C_2 product and ethylene FEs on both Ag-doped Cu and Cu GDEs exhibited an increasing trend with increased applied potentials. This result can be explained by noting that the C–C coupling step for *n*-propanol formation becomes slow at high potential, and thus C_2 intermediate protonation reaction is more favored compared with C–C coupling step for *n*-propanol formation[26,34].

To study the chemical state of the catalyst during CORR, we performed operando X-ray absorption spectroscopy (XAS) of Ag-doped Cu GDE under operando CORR conditions at a constant applied potential of −0.46 V_{RHE}. Operando Cu K-edge X-ray absorption near edge structure (XANES) spectra of Ag-doped Cu GDE show that Cu atoms were reduced to Cu^0 in the first 10 s during CORR (Fig. 3c and Supplementary Fig. 28). Thereafter, the valence state of Cu is maintained at zero throughout CORR. Consistent results are shown in the operando extended X-ray adsorption fine structure (EXAFS). An EXAFS fitting analysis at the Cu K-edge showed the presence of Ag and its strong
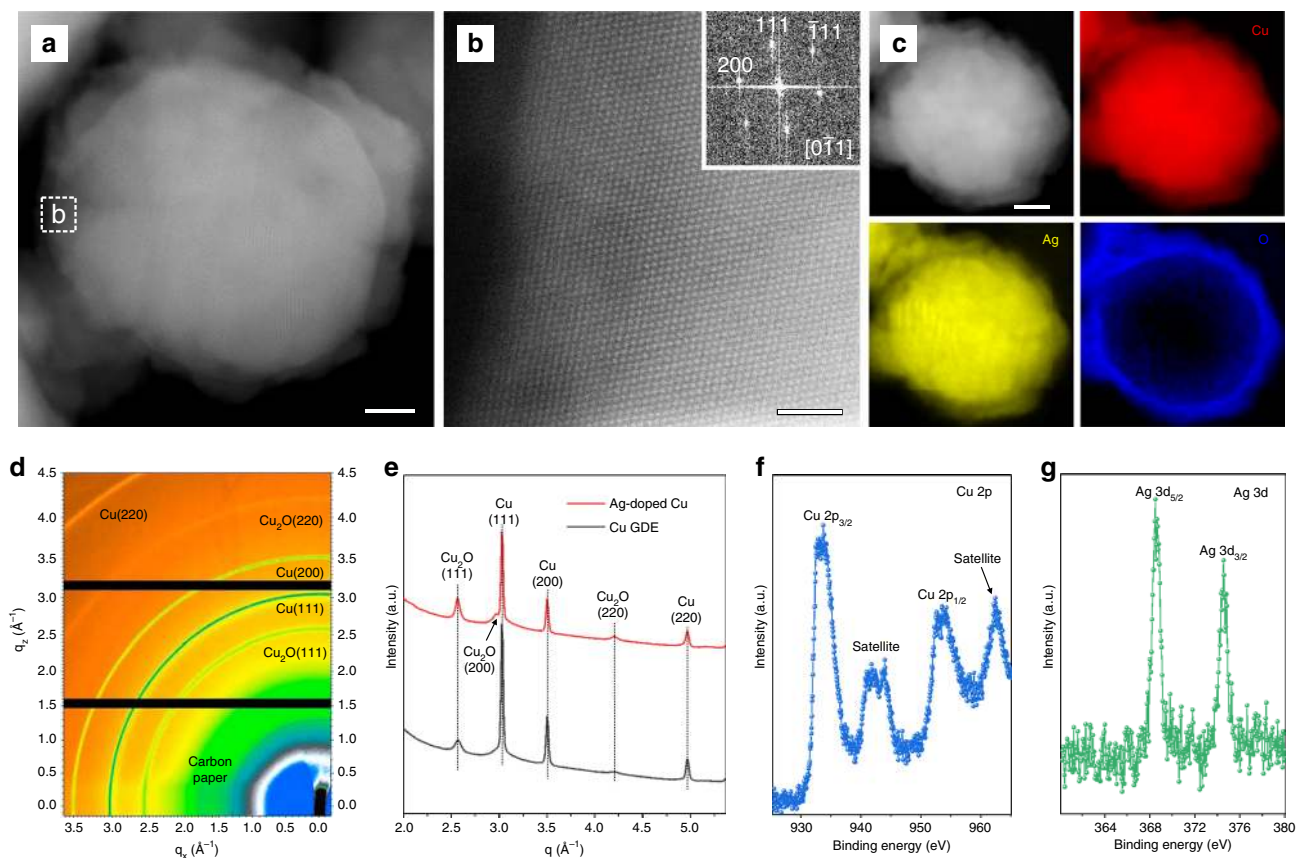
Fig. 2 Structural and compositional analyses of Ag-doped Cu catalyst. **a** High-angle annular dark-field scanning transmission electron microscopy (HAADF-STEM) image taken from a single particle. Scale bar, 20 nm. **b** Atomic-resolution HAADF-STEM image taken from the edge of a nanoparticle marked by a box in (**a**). Inset, the corresponding Fourier transfer image. Scale bar, 2 nm. **c** HAADF-STEM image of an Ag-doped Cu nanoparticle and the corresponding EELS elemental mappings of Cu, Ag, and O. Scale bar, 20 nm. **d**,**e** WAXS map (**d**) and the corresponding sector-average of WAXS map (**e**) for Ag-doped Cu GDE. **f**, **g** High-resolution Cu 2p (**f**) and Ag 3d (**g**) spectra of Ag-doped Cu GDE

interaction with Cu by having Cu–Ag distance value between pure Cu and pure Ag (Fig. 3d and Supplementary Table 11)[13]. Collectively, operando XAS results demonstrated that Ag atoms are doped in the lattice of Cu nanoparticles, and that each element remains in its metallic state during CORR. As a control experiment, we carried out operando Cu K-edge XANES on Cu GDE, and it also showed that Cu oxides were reduced to Cu^0 in the first 10 s during CORR. These results further demonstrated that, rather than benefiting from oxidation states[8,13,16,21,47], the high FE of n-propanol on Ag-doped Cu GDE is associated with metallic states of Cu and might be ascribed to the different structures of Ag-doped Cu relative to Cu.

To explore further the role of Ag doping in Cu in facilitating C_1–C_1 and C_1–C_2 coupling, we investigated the CORR performance of Ag-doped Cu catalysts with different Ag concentrations. To vary the Ag concentration, we changed the immersion time of the Cu GDE in $AgNO_3$ solution to 20 min and 2 h, respectively, denoted Cu–Ag-20 min and Cu–Ag-2 h. As in Ag-doped Cu, both Cu–Ag-20 min and Cu–Ag-2 h catalysts also retained the particle size and the morphology of the pristine Cu nanoparticles (Supplementary Figs. 29–31). Thus, the size and morphology effect can be excluded when comparing the CORR performance between Cu and different types of Ag-doped Cu catalysts. The atomic percentages of Ag doping in Cu were tuned to 2.4% and 7.8% (XPS), respectively, for Cu–Ag-20 min and Cu–Ag-2 h catalysts (Supplementary Figs. 32, 33, and Supplementary Table 6). Relative to Cu GDE, both Cu–Ag-20 min and Cu–Ag-2 h GDE exhibited enhanced FEs of n-propanol, as well as higher

FEs of total C_{2+} products (Fig. 4a, b), in the potential range from −0.36 to −0.56 V_{RHE} toward CORR. These results are in agreement with DFT predictions of enhancement in C_1–C_1 and C_1–C_2 coupling by Ag doping in Cu. Additionally, among Ag-doped Cu catalysts with different Ag concentrations, Ag-doped Cu with an atomic percentage of 4.0% Ag showed the highest n-propanol FE at -0.46 V_{RHE} (Supplementary Fig. 34). The analysis of operando Cu K-edge XANES of Cu–Ag-20 min and Cu–Ag-2 h GDE also demonstrates that Cu oxides are reduced to Cu^0 in the first 10 s during CORR (Fig. 4c) and it is Ag-doped Cu in metallic state that is associated with the enhanced selectivity to n-propanol during CORR.

The carbon-based GDLs suffer from liquid penetration and gas diffusion blockage, termed flooding, over time. To overcome the flooding issue on carbon-based GDE after long operation time, we fabricated the Ag-doped Cu polytetrafluor-oethylene (PTFE) electrode based on a configuration (graphite/carbon nanoparticle/Ag-doped Cu/PTFE electrode) developed by our group[7]. The Ag-doped Cu layer was prepared by immersing a Cu layer in 5 μmol L^{-1} $AgNO_3$ aqueous solution at 65 °C for 1 h. When a potential of −0.46 V_{RHE} was applied, the FE of n-propanol on the Ag-doped Cu PTFE electrode achieved 33% and operated stably over 200 min of CORR (Supplementary Figs. 35 and 36).

We also compared the CO_2RR performance of Ag-doped Cu and pristine Cu to explore whether the asymmetric active sites enhance in this distinct context the C_1–C_1 and C_1–C_2 coupling (Supplementary Fig. 37 and Supplementary Table 12). In the
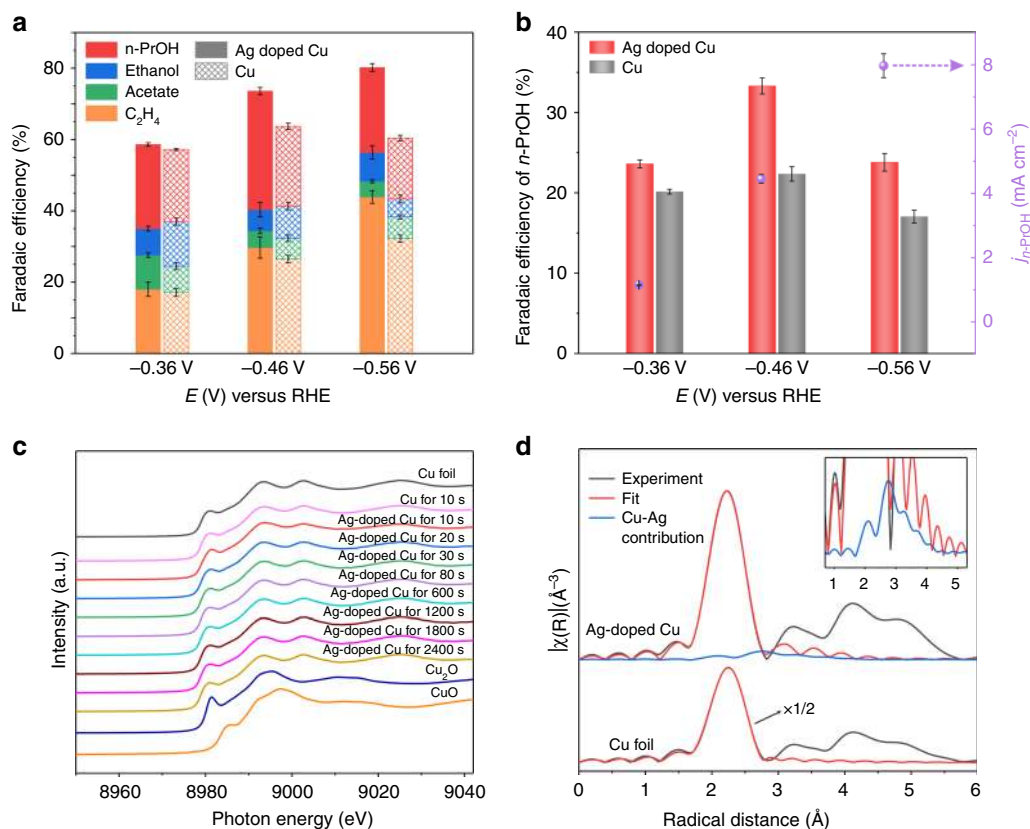
Fig. 3 CO electroreduction performance and operando structural characterizations of Ag-doped Cu catalyst in flow cell. **a** FEs of *n*-propanol (*n*-PrOH), ethanol, acetate, and ethylene on Ag-doped Cu and pristine Cu catalysts under different potentials. **b** Comparison of *n*-propanol FEs on Ag-doped Cu and Cu GDE under different potentials, as well as partial current density of *n*-propanol formation on Ag-doped Cu GDE. Error bars represent the standard deviation based on three separate measurements. **c** Operando Cu K-edge XANES spectra of Cu GDE following 10 s and Ag-doped Cu GDE following 10, 20, 30, 80, 600, 1200, 1800, and 2400 s at −0.46 V_{RHE} during CORR. Bulk Cu foil, CuO, and Cu_2O are listed as references. **d** Operando Cu K-edge EXAFS spectrum of Ag-doped Cu GDE following 10 s at −0.46 V_{RHE} during CORR. Bulk Cu foil was listed as a reference. Inset, an enlarged view of the section from 0.7 to 5.3 Å for Ag-doped Cu GDE
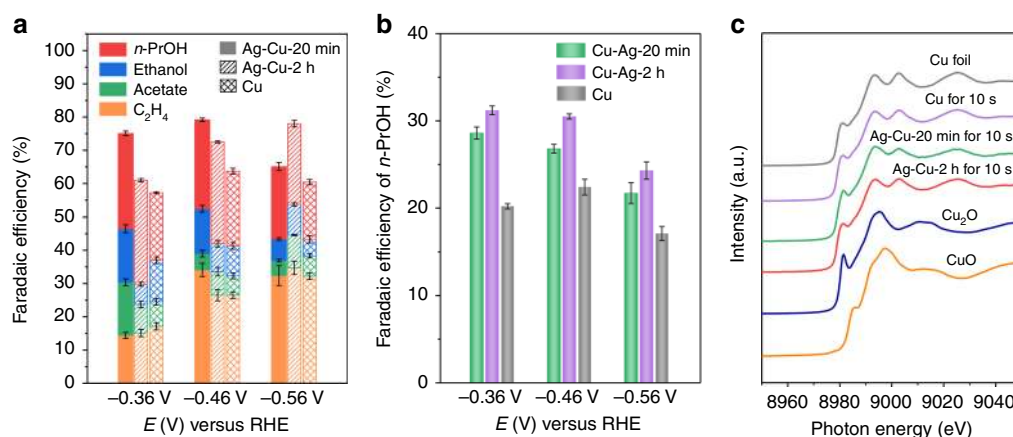
Fig. 4 CO electroreduction performance on different types of Ag-doped Cu catalysts and operando structural characterizations in flow cell. **a** FEs of *n*-propanol, ethanol, acetate, and ethylene on Cu–Ag-20 min, Cu–Ag-2 h, and Cu GDE under different potentials. **b** Comparison of *n*-propanol FEs on Cu–Ag-20 min, Cu–Ag-2 h, and commercial Cu GDE. Error bars represent the standard deviation based on three separate measurements. **c** Operando Cu K-edge XANES spectra of Cu–Ag-20 min, Cu–Ag-2 h, and Cu GDE following 10 s at −0.46 V_{RHE}. Bulk Cu foil, Cu_2O, and CuO are listed as references

potential range from −0.82 to −1.79 V_{RHE} (after *i*R compensation), both C_{2+} and C_3 FEs on Ag-doped Cu catalysts are notably higher than those on pristine Cu: at the potential of −2.96 V_{RHE} (−1.31 V_{RHE} after *i*R compensation), the partial C_{2+} and *n*-propanol current densities of Ag-doped Cu are 308 ± 6 mA cm^{-2} and 36 ± 2 mA cm^{-2}, and C_{2+} and *n*-propanol FEs on Ag-doped Cu are 62 and 7%, respectively, providing a doubling compared to pristine Cu.

Discussion

This work demonstrates Ag doping in Cu to facilitate C_1–C_1 and C_1–C_2 coupling and thus improve the selectivity to C_3 products during CORR. DFT results show that the strain and ligand effects due to Ag doping jointly provide an asymmetric C–C coupling active site containing two neighboring Cu atoms with different electronic structures, and that these are capable of enhancing C_1–C_1 and C_1–C_2 coupling. Experimentally, we achieved a total C_{2+} FE of about 80% and a record n-propanol FE of $(33 \pm 1)\%$ with a partial n-propanol current density $(4.5 \pm 0.1) \, mA \, cm^{-2}$ on Ag-doped Cu catalyst in CORR. The $EE_{cathodic \, half-cell}$ for n-propanol also reaches 21% at a low potential of 0.416 V_{RHE}, with a low overpotential of 0.616 V. These findings provide a framework for rational catalyst design for tuning the CORR selectivity towards high-energy-density C_3 liquid products, a crucial step in overcoming the bottleneck of the electroproduction of C_3 products.

Methods

DFT calculations. In this work, all the DFT calculations were carried out with a periodic slab model using the Vienna ab initio simulation program (VASP) (https://www.vasp.at/). Detailed theoretical methods are found in the Supplementary Information.

Preparation of electrodes. A commercial Cu of 8.5 mg was dispersed in a mixture of 0.85 mL of methanol and 8.5 μL of 5% Nafion under ultrasonication for 30 min. The suspension was deposited on a carbon-based GDL using spray-coating with a catalyst loading of ≈1 mg cm^{-2} to prepare the Cu GDE. We then immersed the prepared Cu GDE in 5 μmol L^{-1} AgNO$_3$ aqueous solution at 65 °C for a certain time period to prepare Ag-doped Cu GDE as cathodes. The main goal of the work was to focus on improving the efficiency of the cathodic side of CORR to propanol. Thus, we used Ni foam (1.6 mm thickness, MTI Corporation) as the oxygen evolution reaction (OER) catalyst in the anode side because it is commercially available and have been showed as a good OER catalyst[48]. Details of chemicals and materials information are found in the Supplementary Information.

Characterization. Scanning electron microscopy (SEM) images were taken using a Quanta FEG 250 microscope (Certain commercial equipment, instruments, or materials are identified in this paper and Supplementary Information in order to specify the experimental procedure adequately. Such identification is not intended to imply recommendation or endorsement by the National Institute of Standards and Technology, nor is it intended to imply that the materials or equipment identified are necessarily the best available for the purpose). HAADF-STEM images were taken using an aberration-corrected FEI Titan 80–300 kV TEM/STEM microscope at 300 kV, with a probe convergence angle of 30 mrad and a large inner collection angle of 65 mrad to provide a nominal image solution of 0.7 Å. EELS elemental mapping was collected on aberration-corrected JEOL JEM-ARM200F electron microscope at 200 kV equipped with Gatan GIF quantum energy filters. Structural characterization of cathodes was obtained using XRD (MiniFlex600) with Cu-Kα radiation. The surface compositions of cathodes were determined by XPS (model 5600, Perkin-Elmer) using a monochromatic aluminum X-ray source. Operando XAS measurements were conducted at 9BM beamline at Advanced Photon Source (APS, Argonne national laboratory, IL). Athena and Artemis software included in a standard IFEFFIT package were used to process XAS data[49]. WAXS measurements were carried out in transmission geometry at the CMS beamline of the National Synchrotron Light Source II (NSLS-II), a U.S. Department of Energy (DOE) office of the Science User Facility operated for the DOE Office of Science by Brookhaven National Laboratory. Samples were measured with an imaging detector at a distance of 0.177 m using X-ray wavelength of 0.729 Å. Nika software package was used to sector average the 2D WAXS images[50]. Data plotting was done in Igor Pro (Wavemetrics, Inc., Lake Oswego, OR, USA).

Electrochemical measurements. All the electrochemical measurements were conducted in flow cell reactor. Electrocatalytic measurements were operated using the three-electrode system at an electrochemical station (AUT50783). In the flow cell reactor, the prepared GDEs, anion exchange membrane, and nickel foam were positioned and clamped together between silicone gaskets and PTFE flow fields. Then 10 mL of electrolyte (1 M KOH aqueous solution) was introduced into the anode chamber between anode and membrane, as well as the cathode chamber between membrane and cathode, respectively. The electrolytes in cathode and anode were circulated by two pumps at the rate of 10 mL min^{-1}. CO gas (Linde, 99.99%) or CO$_2$ gas (Linde, 99.99%) was continuously supplied to gas chamber located at the back side of cathode GDE at the rate of 50 mL min^{-1}. Gas could diffuse into the interface between cathode and electrolyte, thus generating a triple-phase interface between gas, electrode, and electrolyte. The catalytic performance of cathodes was evaluated by performing potentiostatic electrolysis.

All potentials were measured against an Ag/AgCl reference electrode (3 M KCl, BASi). Gas and liquid products were respectively analyzed using gas chromatograph (PerkinElmer Clarus 600) equipped with thermal conductivity and flame ionization detectors, and NMR spectrometer (Agilent DD2 600 MHz) by taking dimethylsulfoxide (DMSO) as an internal standard. All the potentials were converted to values with reference to RHE using
$$E_{RHE} = E_{Ag/AgCl} + 0.210 \, V + 0.0591 \times pH.$$

ECSA was determined based on the equation $ECSA = R_f S$, where R_f was roughness factor and S was geometric area of electrode (1 cm^{-2}). $R_f = C_{dl}/29 \, \mu F \, cm^{-2}$, where C_{dl} is the double-layer capacitance of catalyst and the double-layer capacitance of a smooth Cu surface is assumed to be 29 μF cm^{-2} (ref. [21]). Double-layer capacitances of catalysts were determined by measuring cyclic voltammetry (CV) with different scan rates (40, 60, 80, 100, 120, and 140 mV s^{-1}, respectively) in the potential ranges between 0.20 and 0.24 V_{RHE} where no Faradaic process occurred. The CV measurement was operated in the same flow cell reactor and 1 M KOH aqueous solution saturated with nitrogen (Linde, 99.998%) was used as the electrolyte. The flow cell reactor was filled with electrolyte prior to the CV measurement and the electrolyte was not circulated during the CV measurement. N$_2$, instead of CO$_2$, was continuously supplied to gas chamber of the cell. By plotting the average current j ($j = (j_a - j_c)/2$, where j_a and j_c are anodic and cathodic current densities, respectively) at 0.22 V_{RHE} against the scan rate, C_{dl} value was given by the slope.

The electrochemical impedance spectroscopy (EIS) technique was used to measure the ohmic loss between the working and reference electrodes and 70% iR compensation was applied to correct the potentials manually.

Data availability

The data supporting this study are available in the paper and the Supplementary Information. All other relevant source data are available from the corresponding authors upon reasonable request.

References

1. Liu, M. et al. Enhanced electrocatalytic CO$_2$ reduction via field-induced reagent concentration. *Nature* **537**, 382–386 (2016).
2. Gao, S. et al. Partially oxidized atomic cobalt layers for carbon dioxide electroreduction to liquid fuel. *Nature* **529**, 68–71 (2016).
3. Seifitokaldani, A. et al. Hydronium-induced switching between CO$_2$ electroreduction pathways. *J. Am. Chem. Soc.* **140**, 3833–3837 (2018).
4. Le, M. et al. Electrochemical reduction of CO$_2$ to CH$_3$OH at copper oxide surfaces. *J. Electrochem. Soc.* **158**, E45–E49 (2011).
5. Zhang, W. et al. Electrochemical reduction of carbon dioxide to methanol on hierarchical Pd/SnO$_2$ nanosheets with abundant Pd–O–Sn interfaces. *Angew. Chem. Int. Ed.* **57**, 9475–9479 (2018).
6. Qiao, J., Liu, Y., Hong, F. & Zhang, J. A review of catalysts for the electroreduction of carbon dioxide to produce low-carbon fuels. *Chem. Soc. Rev.* **43**, 631–675 (2014).
7. Dinh, C.-T. et al. CO$_2$ electroreduction to ethylene via hydroxide-mediated copper catalysis at an abrupt interface. *Science* **360**, 783–787 (2018).
8. Mistry, H. et al. Highly selective plasma-activated copper catalysts for carbon dioxide reduction to ethylene. *Nat. Commun.* **7**, 12123 (2016).
9. Liu, Y., Chen, S., Quan, X. & Yu, H. Efficient electrochemical reduction of carbon dioxide to acetate on nitrogen-doped nanodiamond. *J. Am. Chem. Soc.* **137**, 11631–11636 (2015).
10. Zhuang, T.-T. et al. Steering post-C–C coupling selectivity enables high efficiency electroreduction of carbon dioxide to multi-carbon alcohols. *Nat. Catal.* **1**, 421–428 (2018).
11. Ren, D., Ang, B. S.-H. & Yeo, B. S. Tuning the selectivity of carbon dioxide electroreduction toward ethanol on oxide-derived Cu$_x$Zn catalysts. *ACS Catal.* **6**, 8239–8247 (2016).
12. Kim, D., Kley, C. S., Li, Y. & Yang, P. Copper nanoparticle ensembles for selective electroreduction of CO$_2$ to C$_2$–C$_3$ products. *Proc. Natl Acad. Sci. USA* **114**, 10560–10565 (2017).
13. Hoang, T. T. H. et al. Nanoporous Copper-silver alloys by additive-controlled electrodeposition for the selective electroreduction of CO$_2$ to ethylene and ethanol. *J. Am. Chem. Soc.* **140**, 5791–5797 (2018).
14. Jouny, M., Luc, W. & Jiao, F. General techno-economic analysis of CO$_2$ electrolysis systems. *Ind. Eng. Chem. Res.* **57**, 2165–2177 (2018).
15. Clark, E. L., Hahn, C., Jaramillo, T. F. & Bell, A. T. Electrochemical CO$_2$ reduction over compressively strained CuAg surface alloys with enhanced multi-carbon oxygenate selectivity. *J. Am. Chem. Soc.* **139**, 15848–15857 (2017).
16. Verdaguer-Casadevall, A. et al. Probing the active surface sites for CO reduction on oxide-derived copper electrocatalysts. *J. Am. Chem. Soc.* **137**, 9808–9811 (2015).

17. Handoko, A. D. et al. Mechanistic insights into the selective electroreduction of carbon dioxide to ethylene on Cu_2O-derived copper catalysts. *J. Phys. Chem. C.* **120**, 20058–20067 (2016).

18. Ren, D. et al. Mechanistic insights into the enhanced activity and stability of agglomerated Cu nanocrystals for the electrochemical reduction of carbon dioxide to n-propanol. *J. Phys. Chem. Lett.* **7**, 20–24 (2016).

19. Rahaman, M., Dutta, A., Zanetti, A. & Broekmann, P. Electrochemical reduction of CO_2 into multicarbon alcohols on activated Cu mesh catalysts: an identical location (IL) study. *ACS Catal.* **7**, 7946–7956 (2017).

20. Jiang, K. et al. Metal ion cycling of Cu foil for selective C–C coupling in electrochemical CO_2 reduction. *Nat. Catal.* **1**, 111–119 (2018).

21. Li, C. W., Ciston, J. & Kanan, M. W. Electroreduction of carbon monoxide to liquid fuel on oxide-derived nanocrystalline copper. *Nature* **508**, 504–507 (2014).

22. Feng, X., Jiang, K., Fan, S. & Kanan, M. W. A direct grain-boundary-activity correlation for CO electroreduction on Cu nanoparticles. *ACS Cent. Sci.* **2**, 169–174 (2016).

23. Raciti, D. et al. Low-overpotential electroreduction of carbon monoxide using copper nanowires. *ACS Catal.* **7**, 4467–4472 (2017).

24. Li, J. et al. Copper adparticle enabled selective electrosynthesis of n-propanol. *Nat. Commun.* **9**, 4614 (2018).

25. Zhuang, T.-T. et al. Copper nanocavities confine intermediates for efficient electrosynthesis of C3 alcohol fuels from carbon monoxide. *Nat. Catal.* **1**, 946–951 (2018).

26. Jouny, M., Luc, W. & Jiao, F. High-rate electroreduction of carbon monoxide to multi-carbon products. *Nat. Catal.* **1**, 748–755 (2018).

27. Kortlever, R., Shen, J., Schouten, K. J. P., Calle-Vallejo, F. & Koper, M. T. M. Catalysts and reaction pathways for the electrochemical reduction of carbon dioxide. *J. Phys. Chem. Lett.* **6**, 4073–4082 (2015).

28. Cheng, T., Xiao, H. & Goddard, W. A. Full atomistic reaction mechanism with kinetics for CO reduction on Cu(100) from ab initio molecular dynamics free-energy calculations at 298 K. *Proc. Natl Acad. Sci. USA* **114**, 1795–1800 (2017).

29. Montoya, J. H., Shi, C., Chan, K. & Nørskov, J. K. Theoretical insights into a CO dimerization mechanism in CO_2. *J. Phys. Chem. Lett.* **6**, 2032–2037 (2015).

30. Liu, S. et al. Shape-dependent electrocatalytic reduction of CO_2 to CO on triangular silver nanoplates. *J. Am. Chem. Soc.* **139**, 2160–2163 (2017).

31. Jhong, H.-R. M. et al. A nitrogen-doped carbon catalyst for electrochemical CO_2 conversion to CO with high selectivity and current density. *ChemSusChem* **10**, 1094–1099 (2017).

32. Gabardo, C. M. et al. Combined high alkalinity and pressurization enable efficient CO_2 electroreduction to CO. *Energy Environ. Sci.* **11**, 2531–2539 (2018).

33. Xiao, H., Cheng, T. & Goddard, W. A. Atomistic mechanisms underlying selectivities in C_1 and C_2 products from electrochemical reduction of CO on Cu (111). *J. Am. Chem. Soc.* **139**, 130–136 (2016).

34. Kuhl, K. P., Cave, E. R., Abram, D. N. & Jaramillo, T. F. New insights into the electrochemical reduction of carbon dioxide on metallic copper surfaces. *Energy Environ. Sci.* **5**, 7050–7059 (2012).

35. Vayenas, C. G., White, R. E. & Gamboa-Aldeco, M. E. *Modern Aspects of Electrochemistry* Vol. 42 (Springer, New York, 2008).

36. Hori, Y., Takahashi, R., Yoshinami, Y. & Murata, A. Electrochemical reduction of CO at a copper electrode. *J. Phys. Chem. B* **101**, 7075–7081 (1997).

37. Loiudice, A. et al. Tailoring copper nanocrystals towards C_2 products in electrochemical CO_2 reduction. *Angew. Chem. Int. Ed.* **55**, 5789–5792 (2016).

38. Lum, Y., Cheng, T., Goddard, W. A. & Ager, J. W. Electrochemical CO reduction builds solvent water into oxygenate products. *J. Am. Chem. Soc.* **140**, 9337–9340 (2018).

39. Pérez-Gallent, E., Figueiredo, M. C., Calle-Vallejo, F. & Koper, M. T. M. Spectroscopic observation of a hydrogenated CO dimer intermediate during CO reduction on Cu(100) electrodes. *Angew. Chem. Int. Ed.* **56**, 3621–3624 (2017).

40. Goodpaster, J. D., Bell, A. T. & Head-Gordon, M. Identification of possible pathways for C–C bond formation during electrochemical reduction of CO_2: new theoretical insights from an improved electrochemical model. *J. Phys. Chem. Lett.* **7**, 1471–1477 (2016).

41. Xiao, H., Goddard, W. A., Cheng, T. & Liu, Y. Cu metal embedded in oxidized matrix catalyst to promote CO_2 activation and CO dimerization for electrochemical reduction of CO_2. *Proc. Natl Acad. Sci. USA* **114**, 6685–6688 (2017).

42. Hussain, J., Jonsson, H. & Skulason, E. Calculations of product selectivity in electrochemical CO_2 reduction. *ACS Catal.* **8**, 5240–5249 (2018).

43. Greeley, J. et al. Alloys of platinum and early transition metals as oxygen reduction electrocatalysts. *Nat. Chem.* **1**, 552–556 (2009).

44. Studt, F. et al. Identification of non-precious metal alloy catalysts for selective hydrogenation of acetylene. *Science* **320**, 1320–1322 (2008).

45. Liu, P. & Norskov, J. K. Ligand and ensemble effects in adsorption on alloy surfaces. *Phys. Chem. Chem. Phys.* **3**, 3814–3818 (2001).

46. Cobley, C. M. & Xia, Y. Engineering the properties of metal nanostructures via galvanic replacement reactions. *Mater. Sci. Eng. R: Rep.* **70**, 44–62 (2010).

47. Zhou, Y. et al. Dopant-induced electron localization drives CO_2 reduction to C_2 hydrocarbons. *Nat. Chem.* **19**, 974–980 (2018).

48. Zhu, W., Zhang, R., Qu, F., Asiri, A. M. & Sun, X. Design and application of foams for electrocatalysis. *Chemcatchem* **9**, 1721–1743 (2017).

49. Ravel, B. & Newville, M. ATHENA, ARTEMIS, HEPHAESTUS: data analysis for X-ray absorption spectroscopy using IFEFFIT. *J. Synchrotron Radiat.* **12**, 537–541 (2005).

50. Jan, I. Nika: software for two-dimensional data reduction. *J. Appl. Crystallogr.* **45**, 324–328 (2012).

Acknowledgements

Author contributions

E.H.S. supervised the project. X.W. designed and carried out the experiments, analyzed the data, and wrote the paper. Z.W. carried out DFT simulations and wrote the corresponding section. J.L., D.-H.N. and F.L. performed synchrotron X-ray spectroscopy measurements. C.-W.H., C.-S.T., Z.C., M.C. and S.-C.L. conducted the aberration-corrected TEM characterizations. C.M.G. performed SEM characterization. P.T. and A.P. carried out XPS measurements. A.R.K. and L.J.R. carried out the WAXS measurement and analysed the WAXS data. T.-T.Z., C.-T.D., A.S., Y.P., Y.W., A.H.I, B.S., A.O., S.O.K. and D.S. assisted with the discussions. All authors discussed the results and contributed to the preparation of manuscript.

Competing interests

The authors declare no competing interests.

Additional information

Correspondence and requests for materials should be addressed to E.H.S.